

Visualizing delocalized correlated electronic states in twisted double bilayer graphene

Canxun Zhang,^{1,2,3,7} Tiancong Zhu,^{1,2,7} Salman A. Kahn,^{1,2,7} Shaowei Li,^{1,2,3} Birui Yang,¹ Charlotte Herbig,¹ Xuehao Wu,¹ Hongyuan Li,^{1,2} Kenji Watanabe,⁴ Takashi Taniguchi,⁵ Stefano Cabrini,⁶ Alex Zettl,^{1,2,3} Michael P. Zaletel,^{1,2*} Feng Wang,^{1,2,3*} and Michael F. Crommie^{1,2,3*}

¹Department of Physics, University of California, Berkeley, CA 94720, USA.

²Materials Science Division, Lawrence Berkeley Laboratory, Berkeley, CA 94720, USA.

³Kavli Energy NanoSciences Institute, University of California, Berkeley, CA 94720, USA.

⁴Research Center for Functional Materials, National Institute for Materials Science, 1-1 Namiki, Tsukuba 305-0044, Japan.

⁵International Center for Materials Nanoarchitectonics, National Institute for Materials Science, 1-1 Namiki, Tsukuba 305-0044, Japan.

⁶Molecular Foundry, Lawrence Berkeley Laboratory, Berkeley, CA 94720, USA.

⁷These authors contributed equally.

*Correspondence to: mikezaletel@berkeley.edu (M. P. Z.); fengwang76@berkeley.edu (F. W.); crommie@berkeley.edu (M. F. C)

Abstract

The discovery of interaction-driven insulating and superconducting phases in moiré van der Waals heterostructures has sparked considerable interest in understanding the novel correlated physics of these systems. While a significant amount of studies have focused on twisted bilayer graphene, correlated insulating states and a superconductivity-like transition up to 12 K have been reported in recent transport measurements of twisted double bilayer graphene (tDBLG). Here we present a scanning tunneling microscopy and spectroscopy (STM/STS) study of gate-tunable tDBLG devices. We observe splitting of the van Hove singularity peak by ~ 20 meV at half-filling of the tDBLG conduction flatband, with suppression of the local density of states at the Fermi level. STS mapping shows that this correlated state is spatially delocalized and has constant energy-splitting across the different regions in the moiré unit cell, inconsistent with a Mott localization picture. We have performed self-consistent Hartree-Fock calculations which suggest that exchange-driven spontaneous symmetry breaking in the degenerate conduction flatband is likely to be the origin of the observed correlated state. Our results provide insight into the nature of electron-electron interactions in tDBLG and related moiré systems.

Main text

The stacking of atomically-thin van der Waals (vdW) materials enables an elegant platform for studying correlated electronic states. Moiré superlattices formed by lattice misalignment between adjacent vdW sheets can create narrow mini-bands with width comparable to or even smaller than the Coulomb interaction energy,^{1,2} leading to the emergence of various correlated phases. Experimental signatures of interaction-driven electronic states in moiré vdW stacks were first observed in magic-angle twisted bilayer graphene (tBLG), where the coexistence of insulating and superconducting phases resembles the phase diagram of high temperature cuprate superconductors.³⁻⁷ More exotic phases, such as orbital ferromagnets and correlated Chern insulators, were later reported in other moiré vdW systems.⁸⁻¹⁵ Transport measurements on twisted double bilayer graphene (tDBLG), which consists of two sheets of Bernal-stacked bilayer graphene with a small rotational misalignment, have shown new correlated features such as enhancement of a correlation gap under external magnetic field and a superconductivity-like critical transition with onset temperature as high as 12 K.¹⁶⁻²⁰ The precise nature of the electronic states in tDBLG, however, remains elusive, and the lack of spatially-resolved electronic structure data creates challenges in modeling its rich correlation physics.

Here we use STM/STS to study the local electronic structure of tDBLG. Fabrication of tDBLG gate-tunable devices allows us to continuously change the carrier density in our samples and to probe their local density of states (LDOS) at different electron filling levels. We observe that the low-energy electronic structure of tDBLG is dominated by two narrow moiré minibands usually referred to as conduction and valence “flatbands” (FBs), each accommodating four electrons per moiré unit cell owing to spin and valley degeneracies. Their energy separation can be tuned by an applied vertical electric field. When the conduction FB is half-filled we observe an interaction-driven suppression of LDOS at the

Fermi level, in agreement with an emergent correlated insulating phase detected in transport studies.¹⁶⁻²⁰ In contrast to the electronic structure of tBLG,^{1,2,21-25} we find that FB wavefunctions in tDBLG are delocalized in real space and that the correlation-induced LDOS reduction is present everywhere in the moiré unit cell. This spatially-extended correlated state suggests that Mott physics, where the insulating phase is caused by strong repulsion between localized electrons, is inadequate to explain correlation effects in tDBLG. Instead, Hartree-Fock calculations based on a continuum model exhibit good agreement with our experimental data and point to a picture where exchange drives spontaneous symmetry breaking of the four-fold degenerate conduction FB in tDBLG, a mechanism more analogous to Stoner or integer quantum Hall ferromagnetism.^{26,27}

Our tDBLG samples were fabricated using a tear-and-stack technique with a hexagonal boron nitride (hBN) substrate. tDBLG stacks were deposited onto a SiO₂/Si wafer to allow back-gating during STM measurements (Methods). Figure 1a shows a sketch of the device scheme and Fig. 1b shows an optical microscope picture of one sample. Samples were annealed in ultra-high vacuum before being loaded into the STM system at $T = 4.7$ K for measurement (Methods). Figure 1d shows a representative STM topographic image. The moiré wavelength of ~ 13 nm corresponds to a local twist angle of $\theta \approx 1.08^\circ$, but the moiré pattern is not perfectly three-fold symmetric due to external strain. Variation of the moiré wavelength in different directions allows us to estimate a strain of ~ 0.2 % in this sample. As seen in Fig. 1d we observe three regions that have different apparent heights within each moiré unit cell. We identify those as the three different possible stacking regions of tDBLG: ABBC, ABCA, and ABAB (sketched in Fig. 1c; see Supplementary Note 1).

To characterize the electronic structure of our sample we performed spatially-resolved dI/dV spectroscopy on tDBLG devices at different gate voltages. Before each set of measurements our STM tips were calibrated against the Cu(111) Shockley surface state to

ensure that they were free of artifacts known to arise from loosely bound adsorbates and clusters. dI/dV spectra for tDBLG devices measured over large bias ranges using calibrated tips always exhibited a strong enhancement of the tunneling signal for $|V_{\text{Bias}}| > 60$ mV (Supplementary Fig. 1), a familiar graphene effect known to arise due to phonon-mediated inelastic tunneling.^{28,29} The signal from the elastic tunneling channel is relatively weak compared to this inelastic signal. We therefore focus primarily on the elastic signal within the bias range -60 mV $< V_{\text{Bias}} < 60$ mV, both because correlation physics is expected to be strongest near $V_{\text{Bias}} = 0$ mV (the Fermi level) and to avoid inelastic broadening effects.³⁰ Figure 1e shows typical dI/dV spectra obtained in the ABBC region over this energy range at different gate voltages. For $V_G = 0$ V we observe a single peak close to the Fermi level which exhibits a full width at half maximum (FWHM) of ~ 15 meV. Due to its energetic narrowness we identify this peak as originating from flatband electronic states and label it as “FB”. For $V_G = 60$ V the sample becomes electron-doped and the FB peak shifts to an energy below the Fermi level. A new peak appears at higher energy for this gate voltage that has larger width than the FB peak. We refer to this new feature as the remote conduction band (rCB). At $V_G = -60$ V a similar broad peak appears below the FB peak that we refer to as the remote valence band (rVB).

In contrast to tBLG, the FB electronic states in tDBLG are delocalized in real space. This can be seen in Fig. 2a which compares point spectra obtained in ABBC (blue), ABCA (purple), and ABAB (orange) stacking regions for a gate voltage of $V_G = 60$ V. Here the FB peak at $V_{\text{Bias}} = 20$ mV is seen to appear in all three regions with similar intensity whereas the rCB peak at $V_{\text{Bias}} = 6$ mV is prominent only in the ABBC stacking region. To better visualize the spatial patterns of the FB and rCB wavefunctions we obtained dI/dV spectroscopy grids over an area containing several moiré unit cells. Figure 2b,c show dI/dV maps obtained at the FB peak energy ($V_{\text{bias}} = -20$ mV) and the rCB peak energy ($V_{\text{bias}} = 6$ mV) plotted using the

same color scale. We observe that the FB signal is highly delocalized with only slight amplitude variation within the moiré unit cell (Fig. 2b). The rCB signal, on the other hand, only has significant amplitude in the ABBC region (Fig. 2c). This is further demonstrated by histograms of the two maps plotted in Fig. 2d,e. The delocalized FB has shallow corrugation, leading to a narrower histogram with a smaller maximum/minimum ratio of dI/dV intensity (Fig. 2d) compared to the more corrugated (i.e., localized) rCB state which has a broader histogram with more weight in the intensity troughs (Fig. 2e). Point spectroscopy and dI/dV mapping performed at $V_G = -60$ V show that the rVB peak is similarly localized at the ABBC region compared to the more delocalized FB peak (Supplementary Fig. 2).

To search for possible signatures of interaction effects, we methodically tuned the filling level of the system by varying the gate voltage and traced the evolution of dI/dV spectroscopic features. Figure 3 shows density plots of dI/dV spectra measured as a function of gate voltage over the range -60 V $< V_G < 60$ V for all three stacking regions (ABBC, ABCA, and ABAB). The relationship between the gate voltage V_G and the filling factor ν (average number of electrons or holes per moiré unit cell) is found to be $\Delta\nu/\Delta V_G \approx 0.09$ V⁻¹ based on the calculated capacitance between the tDBLG layers and the gate electrode (Methods). From Fig. 3d-f we find that the FB peak remains near the Fermi level for -45 V $< V_G < 45$ V. This corresponds to a change of filling factor over the full range $-4 < \nu < 4$. At $V_G = 45$ V (-45 V) the FB electronic structure is fully filled (depleted) and the rCB (rVB) peak can be clearly seen in the dI/dV spectra, as shown in Fig. 3a-c (Fig. 3g-i). Further increasing (decreasing) the gate voltage quickly alters the chemical potential and causes the FB peak to jump away from the Fermi level. In the ABAB region, a weak side peak can also be seen branching out from the main FB peak for 5 V $< V_G < 35$ V (Fig. 3f). Since the FB peak is pinned near the Fermi level over this extended gate voltage range, other features in the dI/dV spectra are not expected to move relative to the Fermi level due to changes in electron filling.

This branching is therefore likely to arise from a different mechanism, such as the application of a vertical electric field E from the back-gate which causes the valence FB to separate from the conduction FB and to shift downward in energy.

The most significant feature in Fig. 3d-f, however, is that the FB peak splits in two with a dip at the Fermi level at around $V_G \approx 22.5$ V ($\nu \approx 2$), as highlighted by the dashed black boxes. We have observed consistent FB peak-splitting at $\nu \approx 2$ in several devices, with the local twist angle θ ranging from 1.05° to 1.17° (see Supplementary Note 2 and Supplementary Fig. 3). To better see the evolution of this splitting under different filling factors, we plot in Fig. 4a a series of dI/dV spectra obtained in the ABBC region over the filling range $1 < \nu < 3$ (11.5 V $< V_G < 33.5$ V). A well-defined single FB peak can be seen for filling factors away from $\nu = 2$ (e.g. for $V_G < 15$ V and $V_G > 30$ V). Over the filling factor range $1.65 < \nu < 2.35$ (19 V $< V_G < 26$ V), however, a dip feature is clearly resolved at the Fermi level. By fitting the dI/dV signal with the sum of two Lorentzian peak functions we are able to extract the magnitude of the energy-splitting δ as a function of filling factor (see Supplementary Note 3 and Supplementary Fig. 4). The splitting in the ABBC region reaches its maximum value of $\delta_{\max} = 18.9 \pm 1.2$ meV at $\nu \approx 2$ and then decreases to 13 ± 1 meV at $\nu \approx 1.7$ and $\nu \approx 2.3$ before the two peaks merge (Fig. 4b blue dots). dI/dV spectra measured in the ABCA and ABAB regions display the same trend (Supplementary Fig. 5), with $\delta_{\max}(\text{ABCA}) = 20.0 \pm 1.2$ meV and $\delta_{\max}(\text{ABAB}) = 20.4 \pm 1.3$ meV (Fig. 4b purple and orange dots). To further illustrate the spatial dependence of the splitting, Figure 4c shows dI/dV spectra measured at $\nu \approx 2$ along a line cut through the entire moiré unit cell. We observe that the overall intensity of the FB peaks remains similar and the dip feature at the Fermi level persists through the ABBC, ABCA, and ABAB sites, as well as the transition regions between them. The Fermi-level LDOS suppression at $\nu \approx 2$ in tDBLG is thus robust and

spatially ubiquitous regardless of the local stacking order.

Our experimental observations can be understood by comparison to a continuum theoretical model of tDBLG. We first carried out band structure calculations using a continuum Hamiltonian for tDBLG^{1,27,31} with an interlayer potential difference U to account for the E -field induced by the back-gate (Methods). Figure 1f shows the calculated band structure at $\nu = 0$ and $U = 0$ along the high symmetry directions of the moiré Brillouin zone. Two narrow, overlapping FBs can be seen near the Fermi level (green and pink curves) that are separated in energy from other bands. The van Hove Singularities of the two bands merge into a single peak in the theoretical LDOS (Fig. 1g), reasonably reproducing the FB peak seen in STS measurements (Fig. 1e). Each FB is four-fold degenerate due to spin and valley degrees of freedom, so the calculated electronic structure also agrees with our experimental observation that the FBs host a total of eight electrons per moiré unit cell (i.e., the range $-4 < \nu < 4$ shown in Fig. 3). The other bands in Fig. 1f are more dispersive (black curves) and produce broader LDOS peaks (Fig. 1g) that nicely replicate the experimental rCB and rVB peaks seen in Fig. 1e.

The unusual spatial localization behavior of the FB and rCB states is also reproduced by the theoretical LDOS at $V_G = 60$ V (Fig. 2f-j). Since STS is most sensitive to the electronic states at the sample surface, we plot the calculated LDOS projected onto the topmost graphene layer to better compare with measurements. The spectral density of the FB peak centered at $\mathcal{E} = -14.8$ meV and the rCB peak centered at $\mathcal{E} = 4$ meV in the theoretical LDOS in Fig. 2f matches the experimental spectra in Fig. 2a quite well. Theoretical LDOS maps at these peak energies (Fig. 2g,h) also qualitatively agree with the corresponding dI/dV maps (Fig. 2b,c). Here the theoretical FB density is seen to be delocalized across the moiré unit cell (Fig. 2g) and the rCB signal concentrates in the ABBC region (Fig. 2h). This behavior is reflected in the theoretical density histograms (Fig. 2i,j) which also reasonably

match the experimental histograms (Fig. 2d,e). Similarly, LDOS calculations at $V_G = -60$ V shown in Supplementary Fig. 2 match our experimental observation of localized rVB behavior. The spatially delocalized FB behavior is robust even when we include wavefunction contributions from the other layers in our calculations (see Supplementary Note 4 and Supplementary Fig. 6).

This model band structure for tDBLG captures the basic experimental electronic structure quite well but is unable to explain correlation effects. This limitation is evident if we compare the gate-dependent dI/dV spectra in Fig. 3d-f to the calculated gate-dependent LDOS in the ABBC, ABCA, and ABAB regions (Supplementary Fig. 7a-c). The theoretical model reproduces most of the experimentally observed features, even including the E -field-induced downward branching of the valence FB in the ABAB region for $V_G > 0$ (see Supplementary Notes 5-6 and Supplementary Fig. 8), but the splitting of the conduction FB at $\nu \approx 2$ ($V_G \approx 22.5$ V) is not seen. This is not surprising since the single-particle level treatment does not include electron-electron interactions and thus cannot capture correlated electronic behavior.

To understand the nature of the correlated state at $\nu \approx 2$, we account for electron-electron interactions within the self-consistent Hartree-Fock approximation (Methods).³² We assume the Coulomb interaction, which is screened by the graphene layers, the hBN/SiO₂ substrate and the metallic STM tip, to take the single-plane-screened form $V(\mathbf{q}) = \frac{e^2}{2\epsilon_{\text{eff}}\epsilon_0q} [1 - \exp(-2qds)]$, where ϵ_{eff} is the effective dielectric constant and d_S is the effective macro tip-sample separation (see Supplementary Note 7). Consistent with the theoretical results of Ref.²⁷, the system can lower its total energy through spontaneous symmetry breaking around $\nu = 2$ with the nature of the broken symmetry depending on the detailed band structure as well as screening parameters ϵ_{eff} and d_S . When screening is weak and

electron-electron interactions are much stronger compared with the bandwidth, the ground state of the system exhibits spin polarization in each valley, while in the weak-interaction regime inter-valley coherence can develop (see Supplementary Note 8 and Supplementary Figs. 9-11). Treating ϵ_{eff} and d_S as phenomenological parameters due to the complex screening environment, we find the best fit for our experimental observations are obtained for $\epsilon_{\text{eff}} = 14$ and $d_S = 50$ nm (these values are physically realistic, as explained in Supplementary Note 7). Here the spin-polarized state is favored over the inter-valley coherent state. Figure 4d,e shows the resulting Hartree-Fock band structure and DOS at $\nu = 2$, in which case the two spin sub-bands of the conduction FB are split over the entire moiré Brillouin zone by ~ 19 meV, indicating spontaneous breaking of spin-rotation symmetry. Due to the finite bandwidth of the conduction FB, however, the actual correlation gap with zero DOS is much smaller than the splitting. Outside the conduction FB, the spin-splitting is insignificant (< 5 meV) and the single-particle band structure is approximately preserved. The Fermi-level DOS suppression seen here agrees with the experimentally observed dip feature, and the suggested spin polarization is also consistent with reported magneto-transport data that shows the correlation gap widening in an in-plane magnetic field.¹⁶⁻¹⁹ To more thoroughly compare Hartree-Fock calculations with STS measurements we plot the theoretical spin-splitting (averaged over the mini-Brillouin zone) as a function of the filling factor (Fig. 4f) and the LDOS at different locations in the moiré unit cell for $\nu = 2$ (Fig. 4g). The largest splitting occurs at $\nu = 2$ and the resulting dip feature is seen to persist across the entire moiré unit cell, consistent with the experimental results in Fig. 4b,c. We note, however, that DOS qualitatively reproducing our experimental data can also be obtained for a larger ϵ_{eff} value (e.g. $\epsilon_{\text{eff}} = 20$) where the inter-valley coherent ground state is favored instead (Supplementary Fig. 11).

The delocalized spatial distribution of the conduction FB and the persistent LDOS

suppression at $\nu \approx 2$ across the moiré unit cell point to a spatially extended correlated state in tDBLG. This result has significant implications for our understanding of electronic correlations in tDBLG and related moiré systems. Metal-insulator transitions in strongly interacting systems often arise from Coulomb repulsion between localized electrons, as exemplified by the Hubbard model, and the resulting Mott insulators are usually anti-ferromagnetic due to super-exchange effects. In the case of tBLG, the localization of low-energy electronic states at the AA stacking site^{1,2,21-25} has consequently motivated application of Mott-based mechanisms to explain the correlation-driven phases,³³⁻³⁶ although a competing narrative has stressed the importance of exchange and the non-trivial topology of the tBLG bands.^{32,37-39} Our observation of delocalized correlated states in tDBLG indicates that Mott-like physics is unlikely to be the origin of the correlated insulating phase in this system. Our Hartree-Fock calculations are consistent with this in that they show strong exchange interactions can cause spontaneous symmetry breaking at $\nu \approx 2$ that lift the degeneracy of the conduction FB and lead to a prominent reduction in the electronic DOS at the Fermi level. This scenario, reminiscent of a Stoner or integer quantum Hall ferromagnet,^{26,40} is a promising candidate for the observed correlated state in tDBLG. Future spin-resolved STM studies could provide definite evidence regarding the spin polarization of the ground state and would have significant implications for the pairing channel of any proximate superconductivity.²⁷

In conclusion, combined STM/STS measurements reveal a correlated electronic state in tDBLG that is induced by electron-electron interactions when the conduction FB is half-filled. In contrast to tBLG, the FB wavefunctions in tDBLG are delocalized in real space and the correlation-driven Fermi-level LDOS suppression is observed everywhere inside the moiré unit cell. A continuum model Hamiltonian under Hartree-Fock treatment shows good agreement with our experimental results and suggests that the observed correlated state

originates from an exchange mechanism instead of Mott physics. These findings provide useful insights into the correlated insulating states and related phenomena observed in other vdW-coupled 2D systems.

Methods

Sample preparation. Samples were prepared using the “flip-chip” method⁴¹ followed by a forming-gas anneal.^{42,43} Electrical contacts onto the heterostructure were made by evaporating Cr (5 nm)/Au (50 nm) through a silicon nitride shadow-mask. The sample surface cleanliness was confirmed with contact-AFM prior to STM measurements. Samples were annealed at 300 °C overnight in ultra-high vacuum before insertion into the low-temperature STM stage.

STM/STS measurements. All STM/STS measurements were performed in a commercial Omicron LT-STM held at $T = 4.7$ K using tungsten (W) tips. STM tips was prepared on a Cu(111) surface and calibrated against the Cu(111) Shockley surface state before each set of measurements to avoid tip artifacts. dI/dV spectra were recorded using standard lock-in techniques with a small bias modulation $V_{\text{RMS}} = 0.4\text{--}2$ mV at 613 Hz. dI/dV maps were collected via constant-current grid spectroscopy. All STM images were edited using WSxM software.⁴⁴

Estimation of carrier density and electric field. The relation between the gate voltage V_G , the carrier density n , and the vertical electric field E was estimated by modelling the back-gate configuration in Fig. 1a as a parallel plate capacitor. Therefore

$$n = \frac{\epsilon_L \epsilon_0 V_G}{ed_D} \quad (1a)$$

$$E = \frac{\varepsilon_{\perp} V_G}{2d_D} \quad (1b)$$

where $d_D = 310$ nm is the thickness of the dielectric layers (hBN and SiO₂), ε_0 is the vacuum permittivity, $\varepsilon_{\perp} \approx 3.5$ is the average perpendicular dielectric constant, and e is the elementary charge. The filling factor ν and the carrier density n are further related by

$$\nu = \frac{\sqrt{3}}{2} n l_M^2 \quad (2)$$

where l_M is the moiré wavelength. As both W and Cu have work functions close to that of graphene, tip-induced band bending effects were not observed in our spectroscopic measurements and thus not included in the above estimation.

Continuum model and single-particle calculations. Our band-structure calculations follow those of Ref.²⁷, which are based on the Bistritzer-MacDonald continuum approach to moiré structures.¹ The Bernal-stacked bilayer graphene is modeled using a four-band tight-binding model with $t_0 = -2.61$, $t_1 = 0.361$, $t_3 = 0.282$, $t_4 = 0.138$, $\Delta = 0.015$ eV.⁴⁵ One bilayer is then rotated by angle θ , and the two bilayers hybridize only through their proximate layers, with intra-sublattice strength $w_0 = 0.075$ eV and inter-sublattice strength $w_1 = 0.1$ eV in the notation of Ref.²⁷. We note that in our convention $\theta = 0$ corresponds to the structure obtained when a single sheet of BLG is torn in half, one half translated without rotation, and the two halves stacked with ABBC-alignment. The resulting continuum model is truncated by keeping all states within a radius of 5 mini-Brillouin zones (BZs) of the mini-BZ Γ -point. The effect of the gate-induced perpendicular electric field is modeled by a constant energy difference $U/3$ between two adjacent layers. To relate U to the physically applied gate voltage V_G and the E -field estimated above, we assume an interlayer spacing of $d = 0.33$ nm and model the tDBLG as a uniform dielectric with $\varepsilon_{\perp} \approx 6.5$, giving $U/eE = 0.15$ nm similar to that reported in Ref.²⁰.

Hartree-Fock calculations. Hartree-Fock calculations are done in a k -space approach analogous to earlier Hartree-Fock studies of tBLG^{32,38,39} and tDBLG.²⁷ Our code is an extension of the tBLG code used in Ref.³². The Hamiltonian takes the form

$$H = H_0 + PH_C P - H_{\text{BLG}}^{\text{ex}} \quad (3)$$

where H_0 is the continuum band Hamiltonian discussed above, H_C is the real-space Coulomb interaction $V(q)$, P denotes projection into some number of moiré bands near charge neutrality, and $H_{\text{BLG}}^{\text{ex}}$ is a single-particle correction to be discussed shortly. The Coulomb matrix elements for H_C are evaluated in the basis of the continuum band structure and projected into the 6 bands nearest to the charge neutrality point per valley and spin, for a total of $4 \times 6 = 24$ bands. When evaluating the Coulomb integrals, we ignore the interlayer spacing d , which is accurate up to corrections of order d/l_M . We note that while small, the neglected d/l_M terms will lead to interlayer screening which modifies the effective U , which may be an interesting direction for future work. Since the BLG tight-binding parameters obtained from DFT already contain the effect of renormalization by the Coulomb interaction on the physics of a single bilayer, we follow Refs.^{32,38} by subtracting off the Hartree-Fock Hamiltonian $H_{\text{BLG}}^{\text{ex}}$ (exchange energy) of two *decoupled* BLG layers at charge neutrality.

We then consider a Slater-determinant ansatz which is diagonal in the mBZ momentum k ,

$$|u\rangle = \prod_{k \in \text{mBZ}} \prod_{j=1}^{n_k} \left(\sum_n u_{k,j}^n c_{k,n}^\dagger \right) |0\rangle \quad (4)$$

Here $c_{k,n}^\dagger$ creates an electron in eigenstate (k, n) of the band structure, while $u_{k,j}^n$'s are the set of variational parameters to be optimized. The total occupation n_k is allowed to vary across the mBZ to account for the presence of Fermi surfaces. In addition to translation invariance,

we constrain the u 's to preserve a spin-symmetry about the S^z axis (ruling out non-colinear magnetism, which is not expected in this model), but do not enforce the valley-U(1) symmetry, allowing for spontaneous inter-valley coherence as has been argued to occur in tBLG.³² Discretizing the model on a 20×20 k -grid, the u 's are iteratively adjusted to minimize the energy $\langle u|H|u\rangle$, using the optimal damping algorithm to achieve Hartree-Fock self-consistency. Solving for the self-consistent Hartree-Fock Hamiltonian $H_{\text{HF}}(\nu, U)$ at each filling ν and electric field U , we then reconstruct DOS and LDOS curves by diagonalizing H_{HF} and converting back to real space using the continuum-model wavefunctions. To account for finite temperature and instrumental broadening effects and avoid spurious spikes due to the numerical discretization of the mini-BZ, the (L)DOS is broadened by convolving with $f(\mathcal{E}, \mathcal{E}') = \frac{2}{\pi\lambda} \left[\cosh \frac{2(\mathcal{E} - \mathcal{E}')}{\lambda} \right]^{-1}$, where $\lambda = 2$ meV for DOS and 4 meV for LDOS. Unless specified, the LDOS is always projected onto the topmost graphene layer to enable comparison with dI/dV spectroscopy.

Data Availability

The experimental data and analyses that support the plots within this paper and the findings of this study are available from the corresponding authors upon reasonable request.

Code Availability

The computer codes that support the plots within this paper and the findings of this study are available from the corresponding authors upon reasonable request.

References

- 1 Bistritzer, R. & MacDonald, A. H. Moiré bands in twisted double-layer graphene. *Proceedings of the National Academy of Sciences* **108**, 12233-12237, doi:10.1073/pnas.1108174108 (2011).

- 2 Trambly de Laissardière, G., Mayou, D. & Magaud, L. Localization of Dirac
Electrons in Rotated Graphene Bilayers. *Nano Letters* **10**, 804-808,
doi:10.1021/nl902948m (2010).
- 3 Cao, Y. *et al.* Correlated insulator behaviour at half-filling in magic-angle graphene
superlattices. *Nature* **556**, 80-84, doi:10.1038/nature26154 (2018).
- 4 Cao, Y. *et al.* Unconventional superconductivity in magic-angle graphene
superlattices. *Nature* **556**, 43-50, doi:10.1038/nature26160 (2018).
- 5 Yankowitz, M. *et al.* Tuning superconductivity in twisted bilayer graphene. *Science*
363, 1059-1064, doi:10.1126/science.aav1910 (2019).
- 6 Codecido, E. *et al.* Correlated insulating and superconducting states in twisted bilayer
graphene below the magic angle. *Science Advances* **5**, eaaw9770,
doi:10.1126/sciadv.aaw9770 (2019).
- 7 Saito, Y., Ge, J., Watanabe, K., Taniguchi, T. & Young, A. F. Independent
superconductors and correlated insulators in twisted bilayer graphene. *Nature Physics*,
doi:10.1038/s41567-020-0928-3 (2020).
- 8 Sharpe, A. L. *et al.* Emergent ferromagnetism near three-quarters filling in twisted
bilayer graphene. *Science* **365**, 605-608, doi:10.1126/science.aaw3780 (2019).
- 9 Lu, X. *et al.* Superconductors, orbital magnets and correlated states in magic-angle
bilayer graphene. *Nature* **574**, 653-657, doi:10.1038/s41586-019-1695-0 (2019).
- 10 Serlin, M. *et al.* Intrinsic quantized anomalous Hall effect in a moiré heterostructure.
Science **367**, 900-903, doi:10.1126/science.aay5533 (2020).
- 11 Cheng, B. *et al.* Fractional and Symmetry-Broken Chern Insulators in Tunable Moiré
Superlattices. *Nano Letters* **19**, 4321-4326, doi:10.1021/acs.nanolett.9b00811 (2019).
- 12 Chen, G. *et al.* Evidence of a gate-tunable Mott insulator in a trilayer graphene moiré
superlattice. *Nature Physics* **15**, 237-241, doi:10.1038/s41567-018-0387-2 (2019).
- 13 Chen, G. *et al.* Signatures of tunable superconductivity in a trilayer graphene moiré
superlattice. *Nature* **572**, 215-219, doi:10.1038/s41586-019-1393-y (2019).
- 14 Chen, G. *et al.* Tunable correlated Chern insulator and ferromagnetism in a moiré
superlattice. *Nature* **579**, 56-61, doi:10.1038/s41586-020-2049-7 (2020).
- 15 Polshyn, H. *et al.* Nonvolatile switching of magnetic order by electric fields in an
orbital Chern insulator. *arXiv e-prints*, arXiv:2004.11353 (2020).
<<https://arxiv.org/abs/2004.11353>>.
- 16 Burg, G. W. *et al.* Correlated Insulating States in Twisted Double Bilayer Graphene.
Physical Review Letters **123**, 197702, doi:10.1103/PhysRevLett.123.197702 (2019).
- 17 Shen, C. *et al.* Correlated states in twisted double bilayer graphene. *Nature Physics*
16, 520-525, doi:10.1038/s41567-020-0825-9 (2020).
- 18 Liu, X. *et al.* Tunable spin-polarized correlated states in twisted double bilayer
graphene. *Nature* **583**, 221-225, doi:10.1038/s41586-020-2458-7 (2020).
- 19 Cao, Y. *et al.* Tunable correlated states and spin-polarized phases in twisted bilayer-
bilayer graphene. *Nature* **583**, 215-220, doi:10.1038/s41586-020-2260-6 (2020).
- 20 He, M. *et al.* Tunable correlation-driven symmetry breaking in twisted double bilayer
graphene. *arXiv e-prints*, arXiv:2002.08904 (2020).
<<https://arxiv.org/abs/2002.08904>>.
- 21 Kerelsky, A. *et al.* Maximized electron interactions at the magic angle in twisted
bilayer graphene. *Nature* **572**, 95-100, doi:10.1038/s41586-019-1431-9 (2019).
- 22 Choi, Y. *et al.* Electronic correlations in twisted bilayer graphene near the magic
angle. *Nature Physics* **15**, 1174-1180, doi:10.1038/s41567-019-0606-5 (2019).
- 23 Xie, Y. *et al.* Spectroscopic signatures of many-body correlations in magic-angle
twisted bilayer graphene. *Nature* **572**, 101-105, doi:10.1038/s41586-019-1422-x
(2019).

- 24 Jiang, Y. *et al.* Charge order and broken rotational symmetry in magic-angle twisted bilayer graphene. *Nature* **573**, 91-95, doi:10.1038/s41586-019-1460-4 (2019).
- 25 Wong, D. *et al.* Cascade of electronic transitions in magic-angle twisted bilayer graphene. *Nature* **582**, 198-202, doi:10.1038/s41586-020-2339-0 (2020).
- 26 Sondhi, S. L., Karlhede, A., Kivelson, S. A. & Rezayi, E. H. Skyrmions and the crossover from the integer to fractional quantum Hall effect at small Zeeman energies. *Physical Review B* **47**, 16419-16426, doi:10.1103/PhysRevB.47.16419 (1993).
- 27 Lee, J. Y. *et al.* Theory of correlated insulating behaviour and spin-triplet superconductivity in twisted double bilayer graphene. *Nature Communications* **10**, 5333, doi:10.1038/s41467-019-12981-1 (2019).
- 28 Zhang, Y. *et al.* Giant phonon-induced conductance in scanning tunnelling spectroscopy of gate-tunable graphene. *Nature Physics* **4**, 627-630, doi:10.1038/nphys1022 (2008).
- 29 Wehling, T. O., Grigorenko, I., Lichtenstein, A. I. & Balatsky, A. V. Phonon-Mediated Tunneling into Graphene. *Physical Review Letters* **101**, 216803, doi:10.1103/PhysRevLett.101.216803 (2008).
- 30 Brar, V. W. *et al.* Observation of Carrier-Density-Dependent Many-Body Effects in Graphene via Tunneling Spectroscopy. *Physical Review Letters* **104**, 036805, doi:10.1103/PhysRevLett.104.036805 (2010).
- 31 Chebrolu, N. R., Chittari, B. L. & Jung, J. Flat bands in twisted double bilayer graphene. *Physical Review B* **99**, 235417, doi:10.1103/PhysRevB.99.235417 (2019).
- 32 Bultinck, N. *et al.* Ground State and Hidden Symmetry of Magic-Angle Graphene at Even Integer Filling. *Physical Review X* **10**, 031034, doi:10.1103/PhysRevX.10.031034 (2020).
- 33 Yuan, N. F. Q. & Fu, L. Model for the metal-insulator transition in graphene superlattices and beyond. *Physical Review B* **98**, 045103, doi:10.1103/PhysRevB.98.045103 (2018).
- 34 Xu, C. & Balents, L. Topological Superconductivity in Twisted Multilayer Graphene. *Physical Review Letters* **121**, 087001, doi:10.1103/PhysRevLett.121.087001 (2018).
- 35 Kang, J. & Vafek, O. Strong Coupling Phases of Partially Filled Twisted Bilayer Graphene Narrow Bands. *Physical Review Letters* **122**, 246401, doi:10.1103/PhysRevLett.122.246401 (2019).
- 36 Seo, K., Kotov, V. N. & Uchoa, B. Ferromagnetic Mott state in Twisted Graphene Bilayers at the Magic Angle. *Physical Review Letters* **122**, 246402, doi:10.1103/PhysRevLett.122.246402 (2019).
- 37 Po, H. C., Zou, L., Vishwanath, A. & Senthil, T. Origin of Mott Insulating Behavior and Superconductivity in Twisted Bilayer Graphene. *Physical Review X* **8**, 031089, doi:10.1103/PhysRevX.8.031089 (2018).
- 38 Xie, M. & MacDonald, A. H. Nature of the Correlated Insulator States in Twisted Bilayer Graphene. *Physical Review Letters* **124**, 097601, doi:10.1103/PhysRevLett.124.097601 (2020).
- 39 Liu, S., Khalaf, E., Lee, J. Y. & Vishwanath, A. Nematic topological semimetal and insulator in magic angle bilayer graphene at charge neutrality. *arXiv e-prints*, arXiv:1905.07409 (2019). <<https://arxiv.org/abs/1905.07409>>.
- 40 Wohlfarth, E. P. The Theoretical and Experimental Status of the Collective Electron Theory of Ferromagnetism. *Reviews of Modern Physics* **25**, 211-219, doi:10.1103/RevModPhys.25.211 (1953).
- 41 Cui, X. *et al.* Low-Temperature Ohmic Contact to Monolayer MoS₂ by van der Waals Bonded Co/h-BN Electrodes. *Nano Letters* **17**, 4781-4786, doi:10.1021/acs.nanolett.7b01536 (2017).

- 42 Au - Jung, H. S. *et al.* Fabrication of Gate-tunable Graphene Devices for Scanning Tunneling Microscopy Studies with Coulomb Impurities. *JoVE*, e52711, doi:doi:10.3791/52711 (2015).
- 43 Garcia, A. G. F. *et al.* Effective Cleaning of Hexagonal Boron Nitride for Graphene Devices. *Nano Letters* **12**, 4449-4454, doi:10.1021/nl3011726 (2012).
- 44 Horcas, I. *et al.* WSXM: A software for scanning probe microscopy and a tool for nanotechnology. *Review of Scientific Instruments* **78**, 013705, doi:10.1063/1.2432410 (2007).
- 45 Jung, J. & MacDonald, A. H. Accurate tight-binding models for the π bands of bilayer graphene. *Physical Review B* **89**, 035405, doi:10.1103/PhysRevB.89.035405 (2014).

Acknowledgements

The authors thank J. Jung, A. Vishwanath, D. Wong, N. Bultinck, J. Y. Lee, E. Khalaf, Y. Chen and G. Wang for helpful conversations. This research was supported by the sp2 program (KC2207) (STM measurement and instrumentation) funded by the Director, Office of Science, Office of Basic Energy Sciences Materials Sciences and Engineering Division, of the U.S. Department of Energy under Contract No. DE-AC02-05CH11231. For graphene characterization we used the Molecular Foundry at LBNL, which is funded by the Director, Office of Science, Office of Basic Energy Sciences, Scientific User Facilities Division, of the US Department of Energy under Contract No. DE-AC02-05CH11231. Support was also provided by National Science Foundation Award DMR-1807233 (device fabrication, image analysis). K.W. and T.T. acknowledge support from the Elemental Strategy Initiative conducted by the MEXT, Japan, Grant Number JPMXP0112101001, JSPS KAKENHI Grant Number JP20H00354 and the CREST(JPMJCR15F3), JST. S.L. acknowledges support from Kavli ENSI Heising Simons Junior Fellowship. C. H. acknowledges the support of Alexander von Humboldt Foundation for a Feodor Lynen research fellowship.

Author contributions

C. Z., S. A. K., C. H. and M. F. C. initiated and conceived the research. C. Z., T. Z., S. A. K., S. L., C. H. and X. W. carried out STM/STS measurements and analyses. M. F. C. supervised STM/STS measurements and analyses. S. A. K., S. L., B. Y., H. L. and S. C. prepared gate-tunable devices. A. Z., F. W. and M. F. C. supervised device preparations. T. T. and K. W. provided the hBN crystals. C. Z., X. W. and M. P. Z. performed band-structure and Hartree-Fock calculations and theoretical analyses. C. Z., T. Z. and M. F. C. wrote the manuscript with help from all authors. All authors contributed to the scientific discussion.

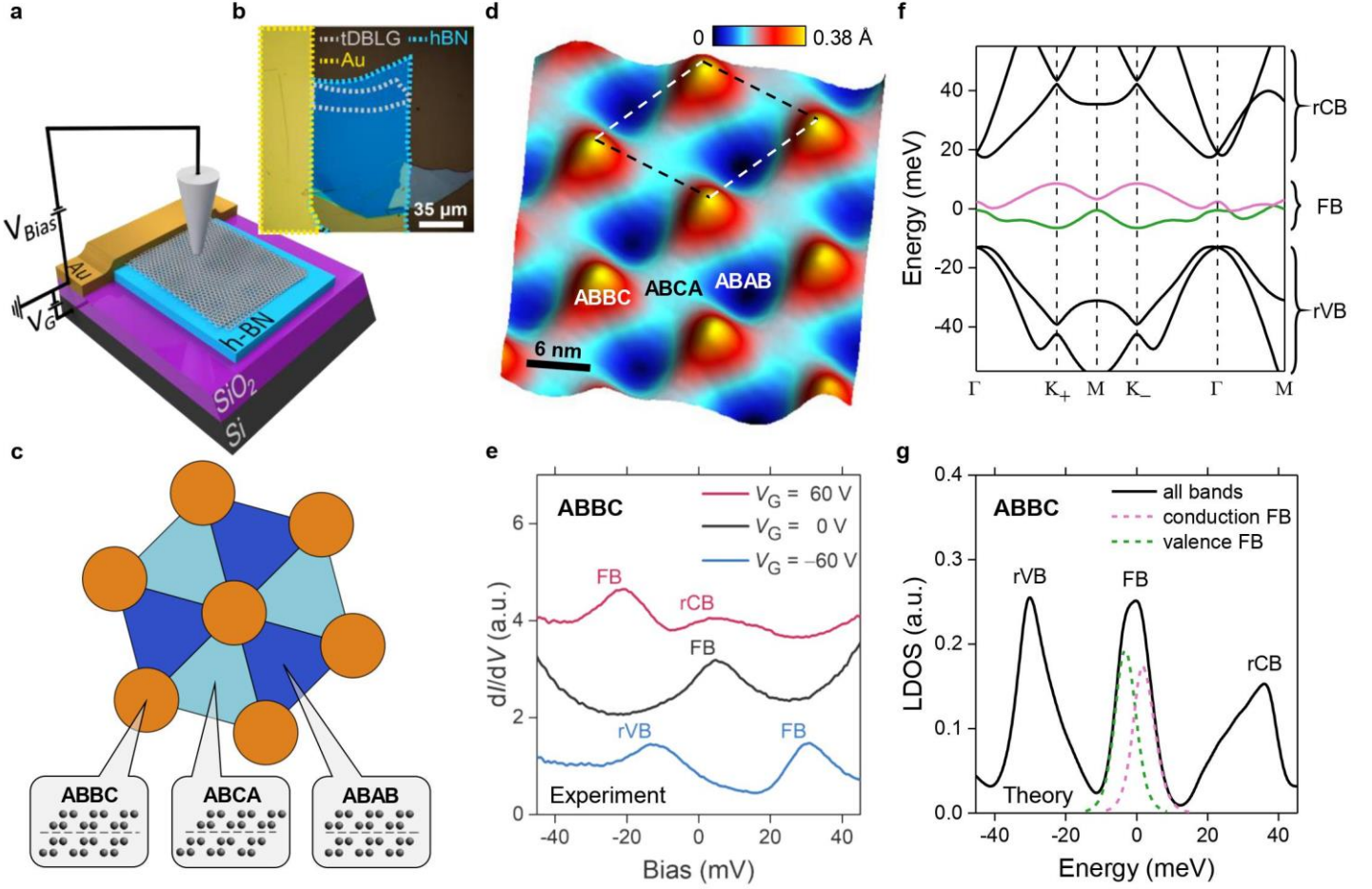


Figure 1: Basic characterization of tDBLG. **a**, STM/STS measurement configuration for tDBLG devices. The doped Si substrate acts as a back-gate to allow tuning of the device carrier density. **b**, Optical microscope image of a tDBLG device. **c**, Sketch of the moiré pattern and three distinct stacking orders for tDBLG. In ABBC stacking the inner two layers of carbon atoms are on top of each other, whereas in ABCA and ABAB stackings they are Bernal-stacked. **d**, STM topographic image of tDBLG with a twist angle $\theta \approx 1.08^\circ$ ($V_{\text{Bias}} = -250$ mV, $I_0 = 0.25$ nA). The dashed box delineate the moiré unit cell. **e**, dI/dV spectra measured in an ABBC region under different back-gate voltages (modulation voltage $V_{\text{RMS}} = 1$ mV; initial $V_{\text{Bias}} = -100$ mV, $I_0 = 0.5$ nA). **f**, Single-particle band structure along the high symmetry directions of the moiré Brillouin zone ($\nu=0$, $U=0$). **g**, Calculated LDOS in an ABBC region. The dashed curves represent the contributions from different flatbands. FB = flatband; rCB = remote conduction band; rVB = remote valence band.

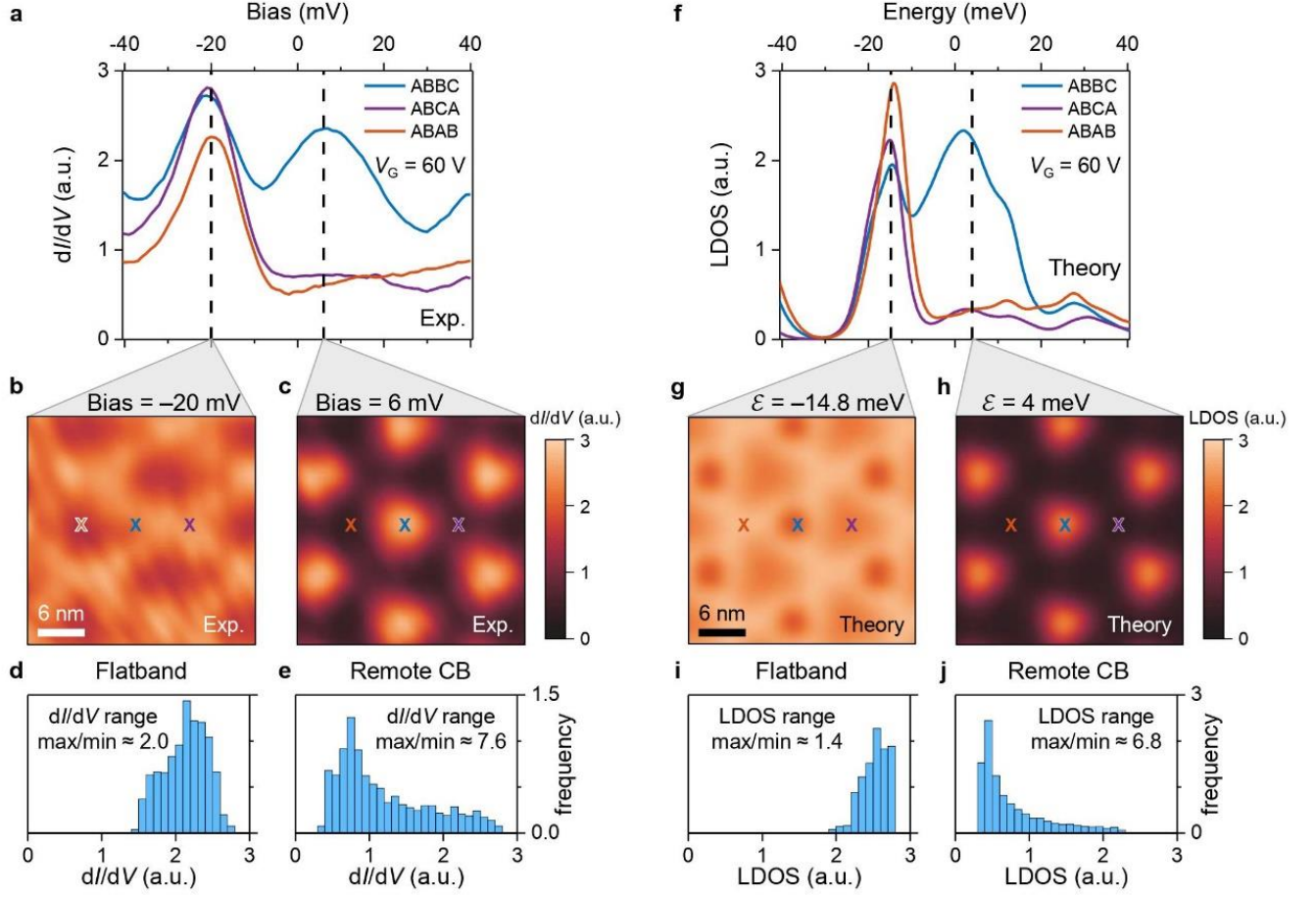


Figure 2: Spatial distribution of flatband and remote conduction band wavefunctions. a, dI/dV spectra for three different stacking regions measured at $V_G = 60$ V. **b, c,** dI/dV maps of the same tDBLG region obtained at **(b)** $V_{\text{Bias}} = -20$ mV and **(c)** $V_{\text{Bias}} = 6$ mV (modulation voltage $V_{\text{RMS}} = 1$ mV; initial $V_{\text{Bias}} = -500$ mV, $I_0 = 2.5$ nA). **d,** Histogram of **(b)**. **e,** Histogram of **(c)**. **f,** Theoretical LDOS of three different stacking regions at $V_G = 60$ V calculated using the single-particle continuum model. **g, h,** LDOS maps at **(g)** -14.8 meV and **(h)** 4 meV. **i,** Histogram of **(g)**. **j,** Histogram of **(h)**. All histograms use bin size of 0.1 a.u. and areas under histograms are normalized to 1.

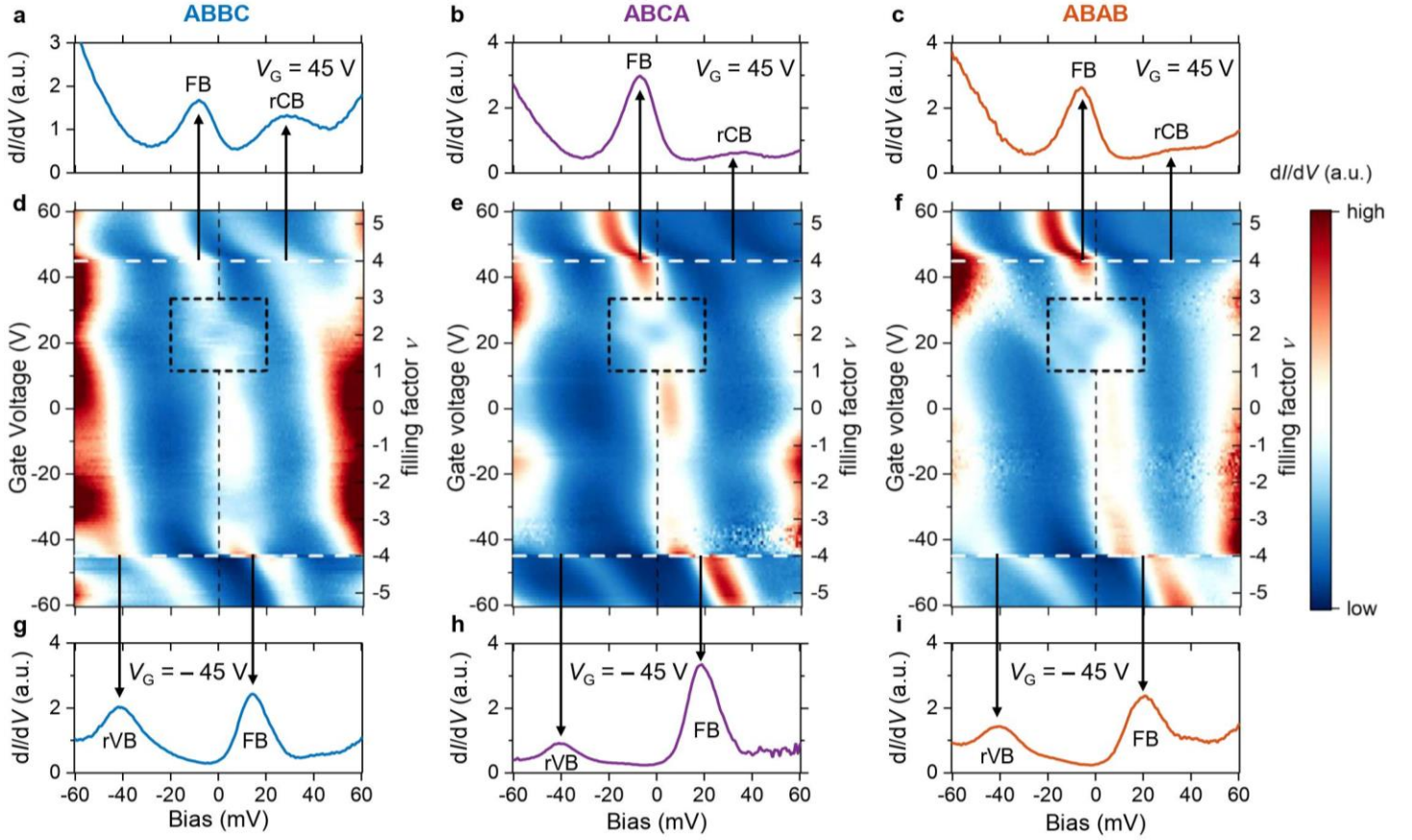


Figure 3: Gate-dependent dI/dV spectroscopy for three stacking regions. **a-c**, dI/dV spectra for three stacking regions at $V_G = 45$ V ($\nu = 4$). **d-f**, Gate-dependent dI/dV density plot for three stacking regions (-60 V $< V_G < 60$ V). The vertical black dashed line denotes zero bias (the Fermi level). The black dashed box highlights the correlation-driven splitting of the FB peak near $\nu \approx 2$. **g-i**, dI/dV spectra for three stacking regions at $V_G = -45$ V ($\nu = -4$). Spectroscopy parameters: modulation voltage $V_{\text{RMS}} = 1$ mV; initial $V_{\text{Bias}} = -100$ mV, $I_0 = 0.5$ nA. FB = flatband; rCB = remote conduction band; rVB = remote valence band.

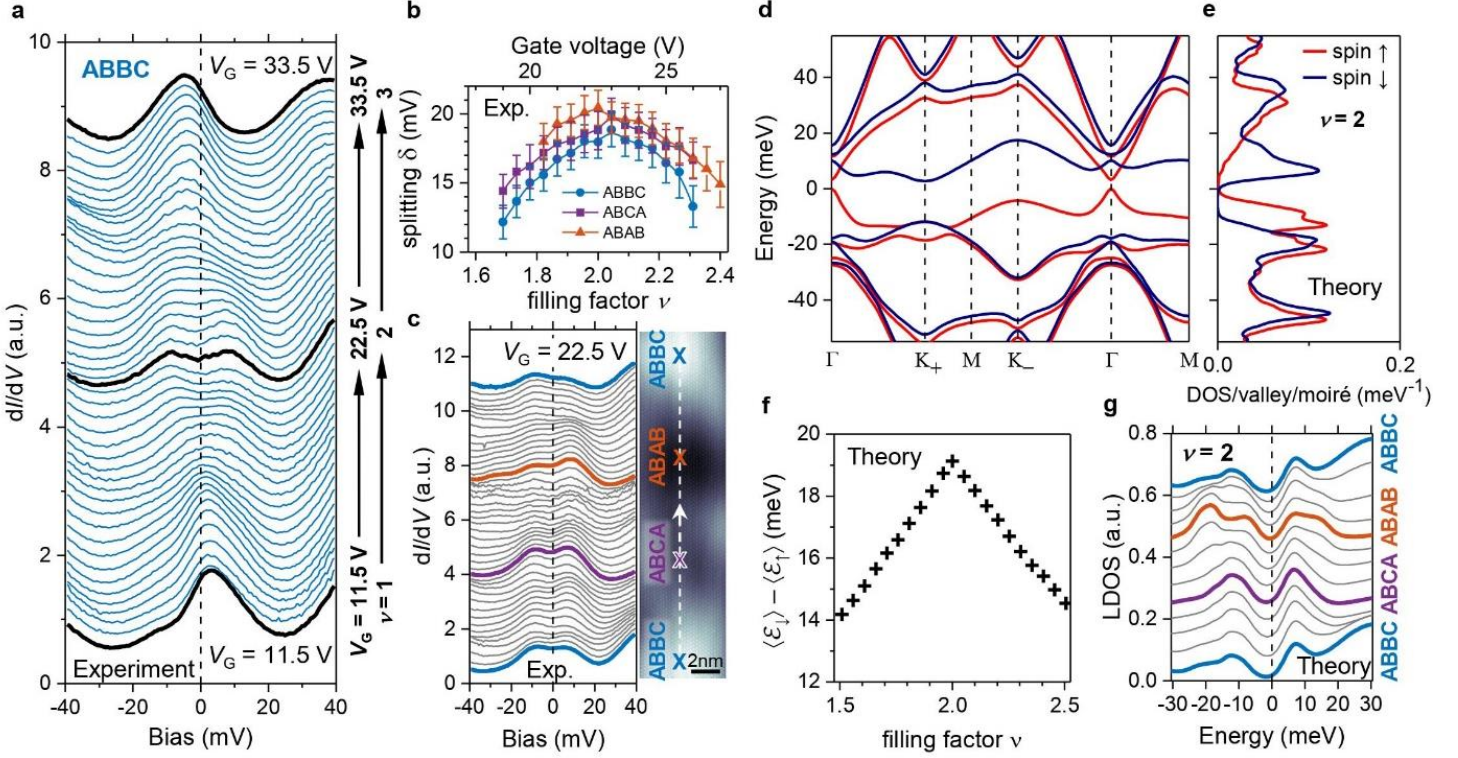


Figure 4: Emergent correlated state at $\nu \approx 2$. **a**, Gate-dependent dI/dV spectra in ABBC region for $11.5 \text{ V} < V_G < 33.5 \text{ V}$ ($1 < \nu < 3$) (modulation voltage $V_{\text{RMS}} = 1 \text{ mV}$; initial $V_{\text{Bias}} = -100 \text{ mV}$, $I_0 = 0.5 \text{ nA}$). **b**, Magnitude of FB energy-splitting with estimated standard deviation extracted as a function of the gate voltage (filling factor) for three stacking regions. **c**, Spatially-resolved dI/dV spectra measured at $V_G = 22.5 \text{ V}$ ($\nu = 2$) along the dashed white line in the topographic image (which goes through all three stacking regions). Scanning parameters: $V_{\text{Bias}} = -100 \text{ mV}$, $I_0 = 0.1 \text{ nA}$. Spectroscopy parameters: modulation voltage $V_{\text{RMS}} = 1 \text{ mV}$; initial $V_{\text{Bias}} = -100 \text{ mV}$, $I_0 = 0.5 \text{ nA}$. **d**, Hartree-Fock band structure of a single valley and **e**, the corresponding spin-resolved DOS for $\nu = 2$ ($U = 20 \text{ meV}$, $\epsilon_{\text{eff}} = 14$, $d_s = 50 \text{ nm}$). Red and blue lines represent spin-up and spin-down sub-bands. **f**, Energy offset (i.e., splitting) between the spin sub-bands averaged over the mini-Brillouin zone as a function of filling factor for $1.5 < \nu < 2.5$. **g**, Calculated Hartree-Fock LDOS for $\nu = 2$ at different positions across the moiré unit cell (the peak at -20 meV in the ABAB region comes from the valence FB, not splitting of the conduction FB).